# Utilization of Non-Conventional Generation Models in Network Analysis

Rui Lopes, Luís Marcelino, Carlos Cardoso
Instituto Superior Técnico

***Abstract*—In this paper, the design and simulation of a 50kW grid connected PV generation system is carried out, with the intent of verifying the compliance of the system with the European norm for grid connection of generators. The designed model has two operating modes: a grid feeding mode, focused on delivering the maximum available power to the grid, and a grid supporting mode: focused on providing controllable power and a response to grid frequency and voltage fluctuations, as well as to voltage dips. A simulation of the system is preformed in Matlab/Simulink in order to verify the model's operation and conformity with the grid connection code.**

***Index Terms*—PV, Grid Connection, Droop Control, Power Control, Fault Ride Though, Grid Fault Support, Frequency Sensitive Mode**

## I. Introduction

Due to recent developments in electronic power converters, as well as environmental concerns, the integration of renewable energies in the electric grid as been growing at a fast pace in recent years. Despite their advantages, the integration of this kind of generators is accompanied by added concerns regarding the quality of service. Due to these concerns, this kind of generators plays an increasingly important role in the contribution to the stability of the grid. Thus, increasingly stricter codes are set on the connection of renewable energy based generators to the electric grid, such as the COMMISSION REGULATION (EU) 2016/631 of 14 April 2016 [1], which establishes a network code on requirements for grid connection of generators.

Thus, the sizing and modelation of a 50kW Photovoltaic (PV) system are carried out in this paper. First, a grid feeding control mode is considered. In this mode the maximum available power is delivered to the electric grid, by means of MPPT techniques coupled with DC link voltage and current controllers. Then a grid supporting control mode is considered, which focuses on delivering controllable power to the grid and on the system's response to frequency and voltage fluctuations, as well as voltage dips. This control mode is realized by means of a current controller, coupled with a power controller and Droop control.

## II. System Design

### A. System Overview

For this paper a two stage topology, consisting of a DC/DC boost converter and an DC/AC converter, was considered, as presented in Fig. 1. The PV array is first connected to a boost converter, which elevates the PV output voltage to a suitable level for the inverter connection. The Boost converter controller is composed of a MPPT controller and a dedicated controlled for operation during voltage dips. The Boost converter is then connected to an inverter that converts the electrical quantities from DC to AC. As mentioned, the control of the inverter has two modes: a grid feeding mode and a grid supporting mode. The inverter is then connected to the electric grid though an LCL output filter and a transformer, at a voltage level of $15kV$.

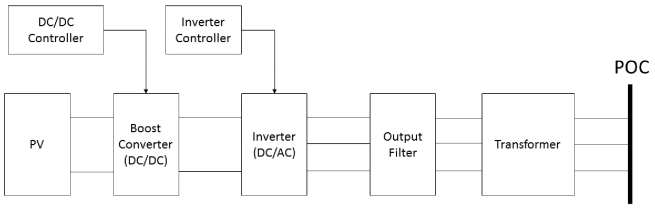


Fig. 1. Two stage grid connected PV system topology.

TABLE I
PV specifications.

| | |
|---|---|
| $P_m$ | $500W$ |
| $V_m$ | $53.94V$ |
| $I_m$ | $9.27A$ |
| $V_{oc}$ | $65.92V$ |
| $I_{sc}$ | $9.77A$ |
| $N$ | 96 |
| $K_I$ | $0.032\%/°C$ |
| $K_V$ | $-0.308\%/°C$ |

### B. PV Array

The panel considered in this work is a 500W 96 Cell Monocrystalline Panel, produced by POWERSYNCH. The PV array is obtained by the association of 100 panels, 20 parallel connections of 5 series connected panels. The data provided by the panel's manufacturer is presented in table I, where $V_{oc}$ and $I_{sc}$ are the open circuit voltage and short circuit current, $V_m$ and $I_m$ are the voltage and current at the maximum power point (MPP) of power $P_m$. $N$ is the number of solar cells in each panel and $K_I$ and $K_V$ are the current and voltage temperature coefficients.

The modelling of the array is done with the 5 parameters model of a solar cell, which can be extended for the panels and array as well. The parameters of this model are the photovoltaic current $I_{ph}$, the diode's inverse saturation current $I_0$ and ideality factor $n$, and the series and shunt resistances

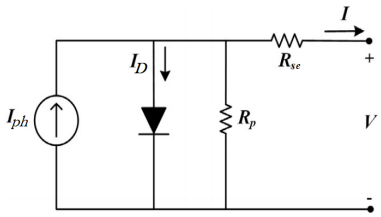


Fig. 2. Electrical circuit of the 5 parameters model of a solar cell [4].

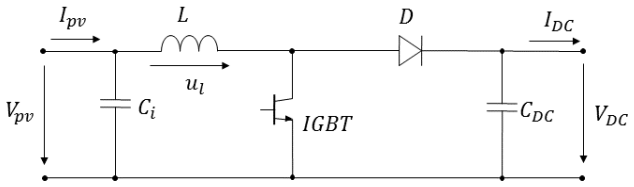


Fig. 3. Boost converter topology.

$R_{se}$ and $R_p$. With these, the equation describing the model's behaviour is presented in 1 [4].

$$I = I_{ph} - I_0(e^{\frac{V+R_{se}I}{nV_t}} - 1) - \frac{V + R_{se}I}{R_p} \tag{1}$$

The first three parameters $I_{ph}$, $I_0$ and $n$ are obtained by [2], [4], [21], [23]

$$I_{ph} = I_{cc} \tag{2}$$

$$I_0 = \frac{I_{ph}}{e^{\frac{V_{co}}{nNV_t}} - 1} \tag{3}$$

$$n = 1.2 \tag{4}$$

where $V_t$ is the diode's thermal voltage, obtained by

$$V_t = \frac{KT}{q} \tag{5}$$

In 5, $K = 1.38 \times 10^{-23} J/K$ is the Boltzman contant, $T$ is the cell's temperature in Kelvin and $q = 1.6 \times 10^{-19} C$ is the electron charge. The resistances are obtained by an iterative method using the expressions [2]

$$P_m = V_m \left[ I_{ph} - I_o(e^{\frac{V_m + R_{se}I_m}{nNV_t}} - 1) - \frac{V_m + R_{se}I_m}{R_p} \right] \tag{6}$$

and

$$R_p = \frac{V_m + R_{se}I_m}{I_{ph} - I_o(e^{\frac{V_m + R_{se}I_m}{nNV_t}} - 1) - \frac{P_m}{V_m}} \tag{7}$$

Starting with a low value, $R_{se}$ is incremented at each iteration, and a corresponding $R_p$ and $P_m$ are calculated. The process is then repeated until the calculated power by 6 matches the panel's nominal power. The photovoltaic current is then adjusted according to [23]

$$I_{ph} \approx \frac{R_p + R_{se}}{R_p} I_{cc} \tag{8}$$

However, the calculated parameters are for Standard Test Conditions (STC: $G = 100W/m^2$, $T = 25°C$). In order to consider the influence of irradiance $G$ and temperature $T$ conditions on the parameters, equations 9 and 10 are used [2].

$$I_{ph} = \frac{G}{G^{STC}}(I_{ph}^{STC} - K_I(T - T^{STC})) \tag{9}$$

$$I_o = I_o^{STC} \left( \frac{T}{T^{STC}} \right)^3 e^{\frac{qE_g}{nK}\left(\frac{1}{T^{STC}} - \frac{1}{T}\right)} \tag{10}$$

where $E_g = 1.12$ is the diode's semiconductor energy gap [2].

At last, in order to scale the panel model to an array, standard voltage and current series and parallel equations are used, resulting in

$$I_{pv} = N_p I_{ph} - N_p I_o(e^{\frac{V_{pv} + R'_{se}I_{pv}}{nV_t}} - 1) - \frac{V_{pv} + R'_{se}I_{pv}}{R'_p} \tag{11}$$

where $I_{pv}$ and $V_{pv}$ are the array's output current and voltage, $N_s$ and $N_p$ are the number of series and parallel connected panels, and $R'_{se}$ and $R'_p$ are the equivalent series and parallel array resistances, given by [2]

$$R'_{se} = \frac{N_s}{N_p} R_{se}, \quad R'_p = \frac{N_s}{N_p} R_p \tag{12}$$

### C. Boost Converter

The boost converter topology considered in this paper is presented in Fig. 3. The input inductor $L$ and the DC link capacitor $C_{DC}$ can both be sized considering the triangular approximation of the DC current and voltage ripple [2], [8] by

$$L = \frac{V_{pv}\delta_D T_c}{\Delta i_l} \tag{13}$$

and

$$C_{DC} = \frac{I_{DC}\delta_D T_c}{\Delta v_{DC}} \tag{14}$$

where $T_c$ is the switching period of the converter's semiconductor, $I_{DC}$ is the DC output current at rated conditions, $\delta_D$ is the duty cycle at rated conditions, and $\Delta i_l$ and $\Delta v_{DC}$ are the desired peak to peak magnitudes of the current and voltage ripples.

The input capacitor will affect the dynamic response of the converter to changes in irradiance, being acceptable to size it as half of the DC link capacitor [9].

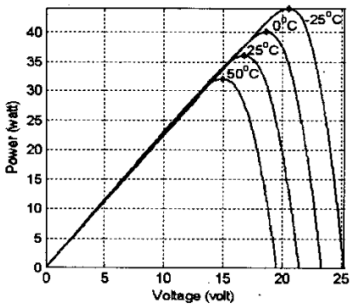


Fig. 4. Influence of temperature on P-V curve of a solar cell [24].

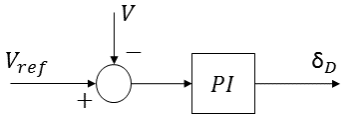


Fig. 5. Boost converter PI controller for FRT operation.

### D. Boost Converter Controller

The designed boost converter controller uses two control modes. The first uses Incremental Conductance (IC) Maximum Power Point Tracking (MPPT) [19] in order to extract the maximum possible power from the PV array under normal grid operating conditions. This method is based on the PV power/voltage curve. An example of this curve is presented in Fig. 4 for several temperatures. As we can see, despite the changes introduced by temperature, the curve will always have a maximum. Thus, the MPP can be found according to 15.

$$\begin{cases} \frac{dP}{dV} > 0, & V < V_m \\ \frac{dP}{dV} = 0, & V = V_m \\ \frac{dP}{dV} < 0, & V > V_m \end{cases} \tag{15}$$

Taking into account that

$$\frac{dP}{dV} = 0 \Leftrightarrow \frac{dI}{dV} = -\frac{I}{V} \tag{16}$$

the difference between these terms can be taken as an error and $\delta_D$ which extract the maximum power can be obtained through an integrator [2].

The second control mode considered is dedicated to Fault Ride Through (FRT) operation. During voltage dips the system's ability to deliver power to the grid is compromised, causing the excess power to be retained in the DC link, leading to overvoltages in the capacitor. Thus, this mode uses a Proportional-Integral (PI) compensator to control the DC link voltage during voltage dips [17], as presented in Fig. 5, where $V_{ref}$ and $V$ are the rated and measured RMS voltage at the Point of Connection (POC).

### E. Inverter

The DC/AC converter here considered was a two level inverter, whose structure is presented in Fig. 6. The inverted is

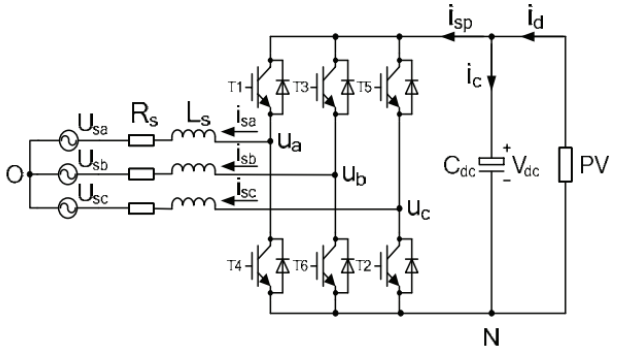


Fig. 6. Topology of a two level inverter [15].

composed of six semiconductors, in parallel with freewheeling diodes, that act as valves and are activated by the inverter controller. $R_s$ and $L_s$ are the equivalent resistance and inductance of the output filter and the transformer used in the connection to the grid. For the purpose of the description of the inverter, a set of symmetric three-phase ideal voltages are assumed

$$\begin{cases} u_{sa} = U_m \cos(\omega t) \\ u_{sb} = U_m \cos(\omega t - \frac{2\pi}{3}) \\ u_{sc} = U_m \cos(\omega t + \frac{2\pi}{3}) \end{cases} \tag{17}$$

In order to prevent short circuits in each of the phase legs of the converter, the semiconductors in each leg are activated in a complementary fashion, and the activation functions $\gamma_k$ ($k = a, b, c$) are defined as 0 when upper switch is conducting and bottom one is OFF, and 1 in the opposite case. Thus, considering the inverter as no neutral cable, the inverter's phase output voltages are given by

$$\begin{cases} u_a = \gamma_a V_{DC} - \frac{\gamma_a+\gamma_b+\gamma_c}{3} V_{DC} \\ u_b = \gamma_b V_{DC} - \frac{\gamma_a+\gamma_b+\gamma_c}{3} V_{DC} \\ u_c = \gamma_c V_{DC} - \frac{\gamma_a+\gamma_b+\gamma_c}{3} V_{DC} \end{cases} \tag{18}$$

As there are $2^3 = 8$ possible combinations of $\gamma_a$, $\gamma_b$ and $\gamma_c$, there will also be 8 possible phase output voltage combinations [14], as presented in table II. With proper modulation, the resulting voltage wave will consist of a fundamental component at grid frequency (50Hz) with the desired amplitude, as well a number of high frequency harmonics, close to the inverter's switching frequency $f_c$. These harmonics are then mitigated by the output filter, resulting in a near sinusoidal output current.

Furthermore, the equations that describe the inverter's behaviour in a three-phase static referential [15] are

$$\begin{cases} u_a = R_s i_{sa} + L_s \frac{di_{sa}}{dt} + u_{sa} \\ u_b = R_s i_{sb} + L_s \frac{di_{sb}}{dt} + u_{sb} \\ u_c = R_s i_{sc} + L_s \frac{di_{sc}}{dt} + u_{sc} \end{cases} \tag{19}$$

From 19, considering the Clarke and Park transformations, the dynamic equations of the inverter in a synchronous rotating frame can be obtained though the transformation matrix

TABLE II
OUTPUT PHASE VOLTAGES OF THE 2 LEVEL INVERTER.

| $\gamma_a$ | $\gamma_b$ | $\gamma_c$ | $V_a$ | $V_b$ | $V_c$ |
|---|---|---|---|---|---|
| 0 | 0 | 0 | 0 | 0 | 0 |
| 1 | 0 | 0 | $\frac{2}{3}V_{DC}$ | $-\frac{1}{3}V_{DC}$ | $-\frac{1}{3}V_{DC}$ |
| 1 | 1 | 0 | $\frac{1}{3}V_{DC}$ | $\frac{1}{3}V_{DC}$ | $-\frac{2}{3}V_{DC}$ |
| 0 | 1 | 0 | $-\frac{1}{3}V_{DC}$ | $\frac{2}{3}V_{DC}$ | $-\frac{1}{3}V_{DC}$ |
| 0 | 1 | 1 | $-\frac{2}{3}V_{DC}$ | $\frac{1}{3}V_{DC}$ | $\frac{1}{3}V_{DC}$ |
| 0 | 0 | 1 | $-\frac{1}{3}V_{DC}$ | $-\frac{1}{3}V_{DC}$ | $\frac{2}{3}V_{DC}$ |
| 1 | 0 | 1 | $\frac{1}{3}V_{DC}$ | $-\frac{2}{3}V_{DC}$ | $\frac{1}{3}V_{DC}$ |
| 1 | 1 | 1 | 0 | 0 | 0 |

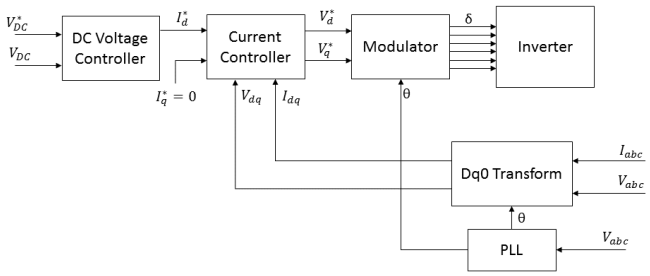


Fig. 7. Grid feeding control structure.

$$T = \frac{2}{3}\begin{bmatrix} \cos(\omega t) & \cos(\omega t - \frac{2\pi}{3}) & cos(\omega t + \frac{2\pi}{3}) \\ -\sin(\omega t) & -\sin(\omega t - \frac{2\pi}{3}) & -sen(\omega t + \frac{2\pi}{3}) \end{bmatrix} \tag{20}$$

the resulting system equations are [15]

$$\begin{cases} i_{sd} = \frac{1}{R_s + sL_s}(U_d - U_{sd} + \omega L_s i_{sq}) \\ i_{sq} = \frac{1}{R_s + sL_s}(U_q - U_{sq} - \omega L_s i_{sd}) \end{cases} \tag{21}$$

### F. Inverter Control

The inverter controller considered has two operating modes. The first, Grid Feeding mode [15], [20], is focused on delivering the maximum available power in the PV array to the grid, and was included in this paper as a way to review more traditional PV technologies, usually employed in low capacity systems. This control mode uses a PI to maintain the DC link voltage at a specified level, thus maintaining the power balance between the DC and AC parts of the system [17]. This, together with the MPPT controller, assures all the available power is delivered to the grid. The grid feeding controller is presented in Fig. 7. In this control mode, the direct component of the current reference in the synchronous reference frame is provided by the DC link voltage controller, while the quadrature component is set to zero in order to assume a power factor of 1. The DC link voltage controller PI is sized using the Symmetrical Optimum Tuning Criteria [3], resulting in expressions 23 and 24 for its proportional

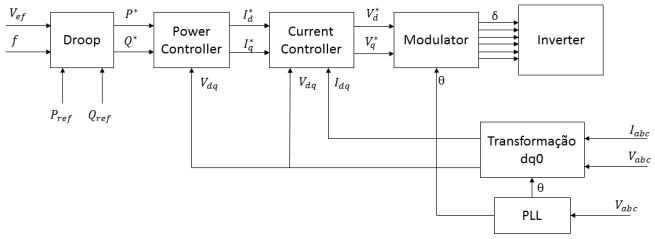


Fig. 8. Grid Supporting control structure.

and integral gains. These, along with the remaining quantities involved in the inverter control, are expressed per unit, with power base the maximum power of the PV array at STC, and the amplitude of the phase voltage and current as base as well. In these, $a$ is a constant that will influence the system's poles, set to 3 in this paper, $T_{eq} = T_s$ is the resulting time constant from a first order approximation of the current controller [3] and $T_{cdc}$ is the DC capacitor's time constant.

$$T_{iv} = a^2 T_{eq} \tag{22}$$

$$K_{pv}^{pu} = \frac{T_{cdc}}{\sqrt{T_{iv} T_{eq}}} \tag{23}$$

$$K_{iv}^{pu} = \frac{K_{pv}^{pu}}{T_{iv}} \tag{24}$$

On the other hand, in the Grid Supporting mode [20], [25], presented in Fig. 8, the dq current reference is provided by an open loop power controller, based on the following analytical power equations in a synchronous reference frame [7], [25]

$$\begin{bmatrix} I_d^* \\ I_q^* \end{bmatrix} = \frac{2}{3}\frac{1}{V_d^2 + V_q^2}\begin{bmatrix} V_d & V_q \\ V_q & -V_d \end{bmatrix}\begin{bmatrix} P^* \\ Q^* \end{bmatrix} \tag{25}$$

The power references used in the power controller are obtained by a Droop Controller [5], [10], [16], [25]. This is a well established method in the regulation of conventional synchronous generator, which may also be here applied. The Droop Controller obtains the active and reactive power references by comparing the frequency and voltage levels to their rated ones, thus ensuring a response to fluctuations of grid frequency and voltage. The Droop Control structure is presented in Fig. 9. The factors $k_P$ and $k_Q$ are factors adjusted in order to obtain the desired response to grid frequency and voltage variations.

The Grid Supporting Controller also has FRT capability. This is achieved by, whenever a voltage dip is detected, generating the dq current references directly as a function of the fault's residual voltage [17]. This mode is presented in more detail ahead with the required minimum reactive current production curve.

Both control modes implemented use the same PI based current controller in synchronous reference frame [3], [15], [25]. This controller is based on the inverter's dynamic equations presented in 21. In these, a strong coupling between the dq

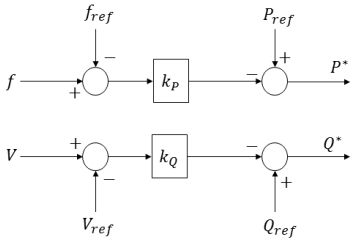


Fig. 9. Droop controller structure.

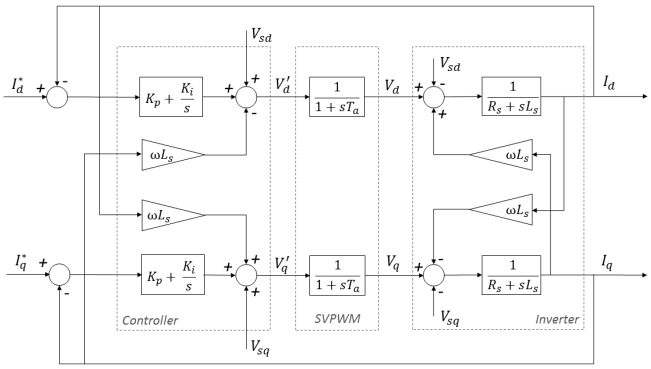


Fig. 10. System representation from a current control point of view.

components of the inverter output current is noticed, thus, in order to overcome this drawback, a feedforward decoupling strategy [3], [15] is considered, allowing for the independent control of the direct and quadrature components of the current, and, as a result, of the active and reactive power. The overall system from a current control point of view is represented in Fig. 10. In here, the modulation was considered as a delay, with a time constant $T_a$ equal to the double of the switching period $T_s$. The current controller is sized using the Modulus Optimum Tuning Criterion [3], resulting in the PI gains in 26, for a damping factor $\zeta = 0.707$. In these, $T_a = T_s/2$ is the time constant associated with the modulation delay and $\tau^{pu} = \frac{L_s^{pu}}{\omega_b R_s^{pu}}$ is the per unit time constant of the equivalent output RL series.

$$\begin{cases} K_p^{pu} = \frac{\tau^{pu} R_s^{pu}}{2T_a} \\ K_i^{pu} = \frac{K_p^{pu}}{\tau^{pu}} = \frac{R_s^{pu}}{2T_a} \end{cases} \tag{26}$$

The current controller then generates a voltage reference in the synchronous reference frame, which is fed to a modulator in order to obtain a set of pulses to activate the inverter's switches. This is done with Space Vector Pulse Width Modulation (SVPWM) [14], [18]. This method is based on the possible phase output voltage levels presented in table II. From these, using the Clarke transform matrix

$$C = \frac{2}{3}\begin{bmatrix} 1 & -1/2 & -1/2 \\ 0 & \sqrt{3}/2 & -\sqrt{3}/2 \end{bmatrix} \tag{27}$$

TABLE III
SPACE VECTORS OF THE TWO LEVEL INVERTER.

| **Vetor** | $\gamma_a$ | $\gamma_b$ | $\gamma_c$ | $V_\alpha$ | $V_\beta$ |
|---|---|---|---|---|---|
| 0 | 0 | 0 | 0 | 0 | 0 |
| 1 | 1 | 0 | 0 | $\frac{2}{3}V_{DC}$ | 0 |
| 2 | 1 | 1 | 0 | $\frac{1}{3}V_{DC}$ | $\frac{\sqrt{3}}{3}V_{DC}$ |
| 3 | 0 | 1 | 0 | $-\frac{1}{3}V_{DC}$ | $\frac{\sqrt{3}}{3}V_{DC}$ |
| 4 | 0 | 1 | 1 | $-\frac{2}{3}V_{DC}$ | 0 |
| 5 | 0 | 0 | 1 | $-\frac{1}{3}V_{DC}$ | $-\frac{\sqrt{3}}{3}V_{DC}$ |
| 6 | 1 | 0 | 1 | $\frac{1}{3}V_{DC}$ | $-\frac{\sqrt{3}}{3}V_{DC}$ |
| 7 | 1 | 1 | 1 | 0 | 0 |

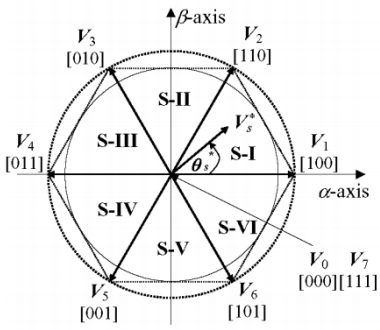


Fig. 11. Space vectors representation in the complex plane [18].

the space vectors in the complex $\alpha\beta$ reference frame, presented in table III, are obtained. A representation of these vectors is presented in Fig. 11. The reference vector $\bar{V}_s$ will rotate along the complex plane in time, through sections **S-I** to **S-VI**, and thus can be approximated by the combination of the vectors that limit the current section. Considering that the reference vector lies between vectors $\bar{V}_k$ and $\bar{V}_{k+1}$, the time that each vector is applied is obtained according to [14], [18]

$$\begin{cases} T_k = \frac{2}{\sqrt{3}} \frac{V_s T_s}{V_k} \sin(k\frac{\pi}{3} - \theta_s) \\ T_{k+1} = \frac{2}{\sqrt{3}} \frac{V_s T_s}{V_k} \sin[\theta_s - (k-1)\frac{\pi}{3}] \end{cases} \tag{28}$$

Should the resulting times be less than the switching period $T_s$, one of the null vectors ($\bar{V}_0$ or $\bar{V}_7$) is applied the remaining time. The resulting modulation index of SVPWM is [14], [18]

$$m = \sqrt{3}\frac{V_s}{V_{DC}} \tag{29}$$

This value will be bounded by the use of a limiter between 0 and 1. In the Grid Supporting mode of operation, this will result in the lower limit of the DC link voltage in the value of

$$V_{DC} = \sqrt{3}V_s \tag{30}$$

allowing the operation of the generator without direct DC link voltage control.

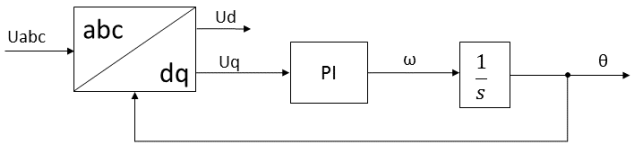


Fig. 12. Synchronous reference frame phase locked loop structure.

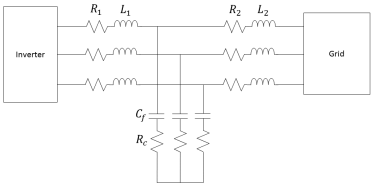


Fig. 13. LCL output filter.

And last, but not least, an integral part of the controller is the Phase Locked Loop (PLL). In this paper, a Synchronous Reference Frame PLL (SRF-PLL) [13] is considered, whose structure is presented in Fig. 12. This control loop is used to measure the POC voltage phase and frequency by means of a PI compensator. It is based on the fact that, when the input and output phases of the PLL are the same, the resulting quadrature component of the voltage is zero *i.e.* the rotating reference frame is in synchronism with the voltage reference [13].

### G. Output Filter

For the output filter, this paper considers a LCL topology [11], [12], [22] as presented in Fig. 13. This filter is well suited for high capacity installations due to smaller component size, comparing to L filters. However, its sizing must be done with added care, for because of its higher order transfer function, it can lead to unwanted resonances which may lead to system instability. The filter also features a damping resistor $R_c$. The filter's transfer function between input voltage and output current resonant frequency is given by

$$f_n = \frac{1}{2\pi}\sqrt{\frac{L_1 + L_2}{L_1 L_2 C_f}} \tag{31}$$

The filter is sized as so the resonant frequency is at least twice the switching frequency, resulting in an attenuation of the current high frequency harmonics. It is also considered that both the grid side and converter size inductors should have the same size *i.e.* $L_1 = L_2$, which leads to a smaller component dimension. This results in

$$L_1 = L_2 = \frac{2}{C_f(\pi f_s)^2} \tag{32}$$

The capacitor is designed in order to obtain a maximum power factor variation of $5\%$, resulting in

$$C_f = 0,05 C_b \tag{33}$$

where $C_b$ is the system's base capacitance. The damping resistor is then sized to one third of the capacitor's impedance at the resonant frequency, that is

$$R_c = \frac{1}{3\omega_n C_f} \tag{34}$$

It is also noteworthy that, at the grid frequency, the impedance of the parallel capacitor as a very high value and thus can be approximated as an open circuit. Taking this into account, the equivalent resistance and inductance used in the current controller tuning, $R_s$ and $L_s$, can be approximated as the sum of the filters grid and converter side resistances and inductances, together with the transformer short circuit impedance.

### H. Transformer

The transformer considered in this paper has rated voltages $15kV/260V$ and a star/delta connection. The transformer's short circuit resistance is of $R_{sc} = 0.0013$ and a short circuit inductance of $L_{sc} = 0.04$. These parameters must be considered in the current controller sizing, which is done according to

$$\begin{cases} L_s^{pu} = L_1^{pu} + L_2^{pu} + L_{sc}^{pu} \\ R_s^{pu} = R_1^{pu} + R_2^{pu} + R_{sc}^{pu} \end{cases} \tag{35}$$

Due to the transformer connection the voltage reference generated by the current controller will have a $\sqrt{3}$ factor in per unit values.

## III. Grid Connection Codes

### A. Response to frequency and voltage fluctuations

The COMMISSION REGULATION (EU) 2016/631 of 14 April 2016 [1] establishes a network code on requirements for grid connection of generators. This document defines grid connection requirements depending on the system's capacity and POC voltage, however, in this paper most of these requirements are considered, even if the system here considered falls out of the category for which the requirements are specified. In this norm, the system's active and reactive power response to frequency and voltage fluctuations is defined.

Firstly, the relevant system operator is to define a $U - Q/P_{max}$ profile within the boundaries of which the generator must be able to provide reactive power at rated capacity. The contour of this profile is presented in [1, Fig. 8], where the Inner Envelope is defined by the relevant system operator and must be confined within the Outer Fixed Envelope.

The norm also defines the Outer Fixed Envelope of the $U - Q/P_{max}$ profile, within which the profile must be contained. This profile and its envelopes are presented in [1, Fig. 9], and the generator must be able to provide reactive power at different active power levels within the specified Inner Envelope.

As for the active power response to frequency fluctuations, *i.e.* Frequency Sensitive Mode (FSM), the European grid code specifies the ranges allowed for the response parameters,

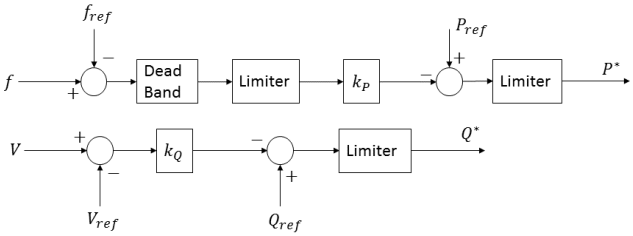


Fig. 14. Altered Droop Controler.

presented in [1, Tab. 5], although in this paper the frequency response insensitivity was not considered. A representative active power response is also presented in [1, Fig. 5], with zero frequency deadband and insensitivity.

In order to meet these requirements, some changes must be made in the Droop Controller in Fig. 9, presented in Fig. 14. First, in the reactive power droop a limiter must be included, which will limit the reactive power provided by the system to the specified envelope maximum and minimum reactive powers, $Q_{max}$ and $Q_{min}$. And second, in the active power droop, a dead zone and two limiters are included. One limiter will bound the demanded active power between zero and the system's maximum capacity, while the other will limit the response's active power range to the specified level. In order to not interfere with operation at lower power levels the second limiter bounds equivalent frequency to which the system will respond, obtained by

$$\Delta F = f_n \frac{s}{100} \frac{\Delta P_1}{P_{ref}} \tag{36}$$

Finally, the Droop parameters $k_P$ and $k_Q$ are determined to obtain the desired response. $k_Q$ is obtained so that the minimum reactive power $Q_{min}$ corresponds to the maximum allowed voltage fluctuation $V_{max}$ by

$$k_Q = \frac{Q_{min}}{V_{ref} - V_{max}} \tag{37}$$

while the parameter $k_P$ is obtained though the desired Droop $s$. However, while the droop is specified in percentage for the system's rated capacity by

$$s = 100 \frac{|\Delta f|}{f_n} \frac{P_{ref}}{|\Delta P|} \tag{38}$$

and the controller operates in p.u. with the installed capacity as base, so $k_P$ is obtained by

$$k_P = 100 \frac{P_{ref}}{P_{max}} \frac{1}{s} = 100 \frac{P_{ref}^{pu}}{s} \tag{39}$$

Furthermore, should the frequency fall of the acceptable operating range of $[47.5, 51.5] Hz$, the dq current references are set to 0, thus effectively shutting down the system.

TABLE IV
SYSTEM PARAMETERS.

| | | | |
|---|---|---|---|
| $P_{max}$ | $50kW$ | $K_p^{pu}$ | 1.14 |
| $I_{ph}$ | $9.7766A$ | $K_i^{pu}$ | 22.25 |
| $I_0$ | $2.118nA$ | $L_1, L_2$ | $71.19\mu H$ |
| $n$ | 1.2 | $R_1, R_2$ | $2m\Omega$ |
| $R'_{se}$ | $0.048\Omega$ | $C_f$ | $150.43\mu F$ |
| $R'_p$ | $71.52\Omega$ | $R_c$ | $162.14m\Omega$ |
| $f_c$ | $5kHz$ | $s$ | 5% |
| $L$ | $9.6mH$ | $Q_{min}^{pu}$ | $-0.45pu$ |
| $C_{DC}$ | $517.87\mu F$ | $Q_{max}^{pu}$ | $0.3pu$ |
| $C_i$ | $258.94\mu F$ | $V_{max}^{pu}$ | $1.05pu$ |
| $f_s$ | $4350Hz$ | $k_P$ | 17 |
| $K_{pv}^{pu}$ | 3.75 | $k_Q$ | 9 |
| $K_{iv}^{pu}$ | 1814.7 | $k_{dip}$ | 2.5 |

### B. Fault Ride Through

In the Dispatch nº9 of the Portuguese General Direction of Energies and Geology of 12/02/2018 [6], the transient requirements for the connection of generators to the electric grid are defined. In this document, along with some requirements already stipulated in the European grid code, the behaviour towards voltage dips of generators is also defined. These will be required to meet the minimum reactive current production curve presented in [6, Fig. 16]. Thus, when a voltage dip is detected, *i.e.* POC voltage less than $0.9pu$, the references of the dq currents are directly generated as a function of the fault intensity. The quadrature component is obtained according to

$$I_q^* = K_{dip}(V - V_{ref}) \tag{40}$$

while the direct component is obtained by

$$I_d^* = 1 - I_q^* \tag{41}$$

The generator will meet the requirements as long as the parameter $K_{dip}$ is larger that its minimum value, obtained from [6, Fig. 16], given by

$$(K_{dip})_{min} = \frac{0.9}{0.4} = 2.25 \tag{42}$$

## IV. RESULTS

A model described system was implemented in Matlab/Simulink. This model has a maximum capacity of $50kW$ and, in Grid Supporting mode, will have a rated power of $0.85pu$ ($45kW$). The model parameters considered and obtained with the equations provided in this paper are presented in table IV. As in the Grid Supporting mode the DC link voltage is not directly controlled, the DC link capacitor $C_{DC}$ was oversized considering a DC link voltage of $800V$. Also, the PV model parameters here presented are obtained in STC and the boost converter components are designed for a 2% ripple both in the Boost Converter input current and DC link voltage.

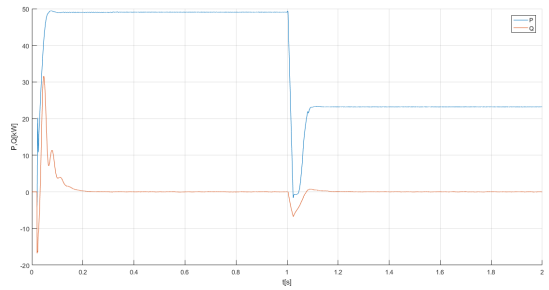

Fig. 15. Active and reactive power in the POC obtained in grid feeding mode under normal grid conditions.

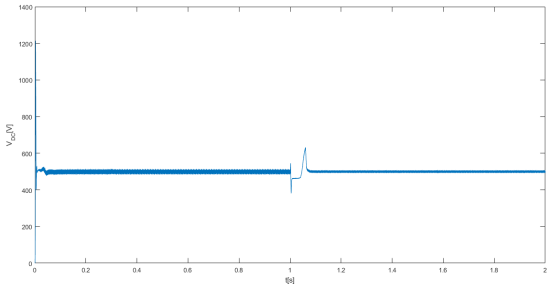

Fig. 16. DC link voltage obtained in grid feeding mode under normal grid conditions.

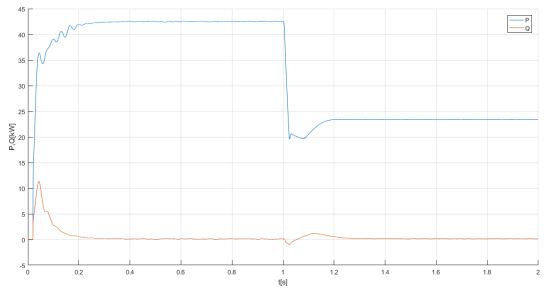

Fig. 17. Active and reactive power in the POC obtained in grid supporting mode under normal grid conditions.

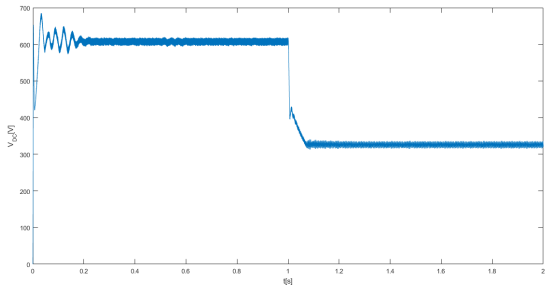

Fig. 18. DC link voltage obtained in grid supporting mode under normal grid conditions.

### A. Grid feeding mode

To verify the operation of the Grid Feeding Controller, a $2s$ simulation was performed, where, for the first second, the PV array is under STC conditions. At $1s$ there is a decrease in irradiance to $500W/m^2$. The results obtained for the active and reactive powers at the POC are presented in Fig. 15, where it can be seen that, under STC conditions, the system injects nearly the maximum power (due to losses) with maximum power factor. After the decrease in irradiance, the MPPT controller finds the new MPP at $23.2kW$. It was also verified that the system injects a near sinusoidal current, with a Total Harmonic Distortion (THD) of $2.07\%$ at STC, and of $4.61\%$ after the decrease in irradiance. In Fig. 16 the obtained DC link voltage is presented, where it can be noted that, apart from a short transient at the moment the irradiance decreases, the controller maintains the voltage at the specified level of $500V$.

### B. Grid supporting mode

The Grid Supporting Controller implemented was tested under the same conditions as the Grid Feeding one, although with the active power reference of $0.85pu$. As it can be seen in Fig. 17, under STC conditions, when the available power is larger than the requested power, the system is able to follow the active power reference, with zero reactive power. After the change in irradiance, the requested power is larger than the available power, and the system provides the maximum available power of $23.2kW$. The current THD measured was $2.24\%$ before the irradiance change and $4.84\%$ after. From Fig. 18 it is noted that, due to the mismatch between requested and available power, the DC link voltage quickly drops to its lower limit of $325.27V$, corresponding to a modulation index of 1. This is not an ideal situation, therefore, there should be a coordination between requested and available power at an higher control level. This can be achieved by the use of daily irradiance/production curves as a means to predict the available power.

The remaining results presented in this paper are obtained under STC conditions, using the Grid Supporting Controller.

### C. Reactive power response

In Fig. 19 the $U - Q/P_{max}$ profile obtained with the implemented model is presented, in which it can be verified that the model has the desired reactive power response to voltage fluctuations, within the specified limits.

In Fig. 20 the $P - Q/P_{max}$ profile is presented, where the capability of the system to provide maximum and minimum reactive power at different active power levels lower than the rated one is tested. It was found that the system has the desired capabilities within the required envelope. During this simulation it was also found that requesting lower power from the system than the available one cause a slight increase in the DC link voltage, although this variation is not nearly as severe as in the opposite case, being the DC voltage when the mismatch is at its largest $663V$.

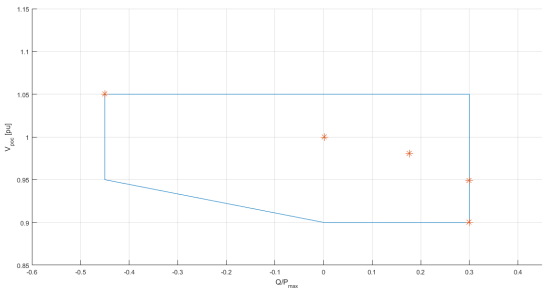

Fig. 19. $U - Q/P_{max}$ profile obtained.

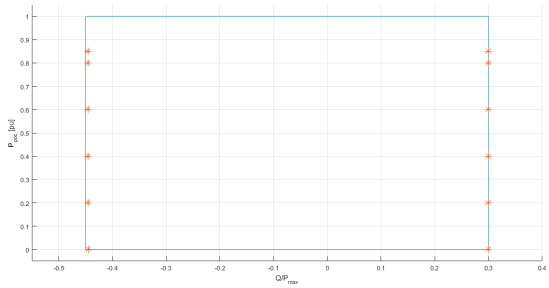

Fig. 20. $P - Q/P_{max}$ profile obtained.

### D. Active power response

In order to display the model's active power response to frequency variations two simulations are presented. The first consist of a ramp overfrequency, during $4s$ beginning at $1s$, for a total increase of $0.6Hz$ over the nominal value, with zero frequency deadband and a maximum active power response of $\frac{\Delta P_1}{P_{max}} = 0.05pu$. It was also considered an active power reference of $80\%$ of its rated value (*i.e.* $0.68pu$ or $34kW$). The power results of this simulation are presented in Fig. 21. Here it is noted that the model begins at the desired power, then, as soon as the frequency variation begins, exhibits an active power decrease, due to the zero frequency deadband. The active power then decreases along with the increase in frequency until the active power limit of $0.05pu = 2.5kW$ is reached, at which point the system will no longer respond to the frequency drop. The Droop $s$ calculated from the results was $5.0748\%$.

The second simulation, here presented in Fig. 22, consists of a ramp underfrequency, taking place from $1s$ until the end of the simulation, with a total frequency decrease of $4Hz$, frequency deadband of $0.5Hz$ and with no active power response limitations. At $0s$ the active power reference is set to $0.6pu$, or $30kW$. Then, after the underfrequency begins, the system will show no response until the frequency deadband is surpassed, moment in which the active power provided will begin to increase linearly until the acceptable frequency operation limit of $45.7Hz$ is reached, when the system stops providing power to the grid. The calculated Droop $s$ in this simulation was $5.0381\%$.

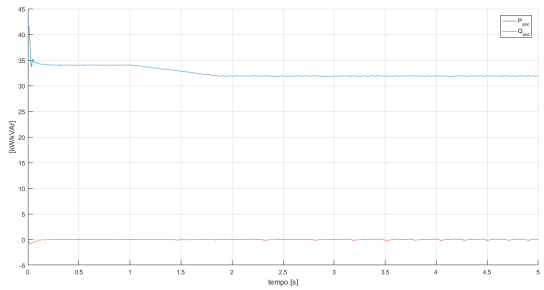

Fig. 21. Active and reactive power results obtained for a $0.6Hz$ overfrequency.

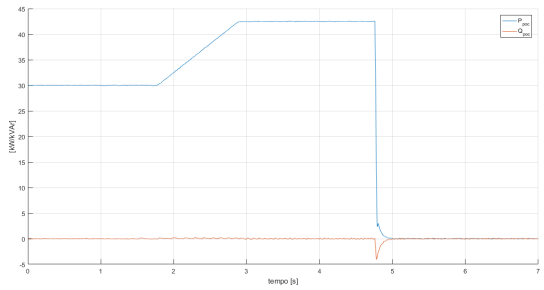

Fig. 22. Active and reactive power results obtained for a $4Hz$ underfrequency.

### E. Fault Ride Through

In order to test the implemented model's FRT capability, the system was subjected to a number of voltage dips of differing intensities. The resulting reactive currents are presented in Fig. 23 as a function of the fault's residual voltage. Here it is noted that, with the selected value of $K_{dip}$, the model will meet the reactive current requirement, and, for faults in which the POC drops below half the rated voltage, the system will operate as a Static Compensator, injecting only reactive current in the POC. It is also noteworthy that, although the system will have FRT capability for near zero voltage, it is not prepared for a total voltage collapse, as in this case the PLL no longer has a sinusoidal voltage from which to obtain a phase. For this situation a dedicated Grid Forming Controller would be required [20].

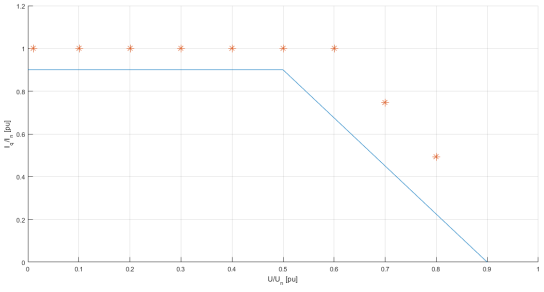

Fig. 23. Reative current production curve during voltage dips obtained.

## V. Conclusion

In this paper, the sizing and modellation techniques of grid connected PV systems was studied. For this purpose, a two stage $50kW$ grid connected PV generator was modelled in Matlab/Simulink. In the DC stage, the PV array was modellated with the 5 Parameter Model, and the MPPT was done with the IC method. In the AC stage, a 2 level inverter was considered, with a controller prepared for operation under Grid Feeding Mode and Grid Supporting Mode. This controller used SVPWM and a PI synchronous current controller with feedforward decoupling to ensure independent active and reactive power control. In Grid Feeding Mode the controller uses DC link voltage control in conjunction with MPPT to ensure the maximum available power is delivered to the grid. In Grid Supporting Mode, the controller uses Droop and Power Controllers to obtain an active and reactive power response to frequency and voltage fluctuations at the POC, as well as direct dq current reference generation as a function of fault intensity to obtain FRT capability. A LCL filter was considered for high frequency current harmonics mitigation.

Overall, the control objectives of this paper were meet, having obtained the desired system response to voltage and frequency variations, as well as voltage dips, according to the Portuguese and European grid connection codes. The influence of the mismatch between available and demanded (*i.e.* reference) powers in the system was also analysed, for which it was found that this mainly affects the DC link voltage. As this voltage is not directly controlled in the Grid Supporting Mode, there should be a coordination between demanded and available powers to ensure the system's proper operation under Grid Supporting mode.

## Acknowledgment

My gratitude towards Prof. Luís Marcelino who mentored the Master Thesis under the context of which this paper was developed. Also, to the Energy Consulting Department of Labelec, where this Thesis was developed under an Internship environment, with a special mention to Eng. Carlos Cardoso, who more closely followed the development of this work, and without whose support this paper would not have been possible.

## References

[1] Commission regulation (eu) 2016/631 of 14 april 2016 establishing a network code on requirements for grid connection of generators. *Official Journal of the European Union*, 4 2016.

[2] Jawairia Atiq. Modelling of a grid connected solar pv system using matlab/simulink. *International Journal of Simulation Systems, Science & Technology*, 17:3, 03 2017.

[3] Chandra Bajracharya and Marta Molinas. Control of vsc-hvdc for wind power. Master's thesis, Norwegian University of Science and Technology, 06 2008. https://ntnuopen.ntnu.no/ntnu-xmlui/handle/11250/256495.

[4] Vun Jack Chin, Zainal Salam, and Kashif Ishaque. Cell modelling and model parameters estimation techniques for photovoltaic simulator application: A review. *Applied Energy*, 154:500–519, September 2015.

[5] Karel De Brabandere, Bruno Bolsens, Jeroen Van den Keybus, Achim Woyte, Johan Driesen, and Ronnie Belmans. A voltage and frequency droop control method for parallel inverters. *IEEE Transactions on Power Electronics*, 22(4):1107–1115, 2007.

[6] Direção Geral de Energia e Geologia. Requisitos transitórios a aplicar na ligação de geradores de eletricidade à rede elétrica de serviço público (resp) de geradores pv e cpv. Despacho n.º 9, 2 2018.

[7] Liu Guihua, Guo Lei, Tao Hailiang, Zhu Xiaohui, and Wang Wei. Pq-u control method of grid-connected pv inverter under weak grid. In *2017 IEEE Transportation Electrification Conference and Expo, Asia-Pacific (ITEC Asia-Pacific)*, pages 1–6, 2017.

[8] B. M. Hasaneen and Adel A. Elbaset Mohammed. Design and simulation of dc/dc boost converter. *2008 12th International Middle-East Power System Conference*, pages 335–340, 2008.

[9] Aamir Hayat, Ali Faisal, Muhammad Yaqoob Javed, M. Hasseb, and Riaz Ahmad Rana. Effects of input capacitor (cin) of boost converter for photovoltaic system. *2016 International Conference on Computing, Electronic and Electrical Engineering (ICE Cube)*, pages 68–73, 2016.

[10] Xing Huang, Xinmin Jin, Tianyi Ma, and Yibin Tong. A voltage and frequency droop control method for microsources. In *2011 International Conference on Electrical Machines and Systems*, pages 1–5, 2011.

[11] A. E. W. H. Kahlane, L. Hassaine, and M. Kherchi. Lcl filter design for photovoltaic grid connected systems. 2015.

[12] Emre Kantar, S. Nadir Usluer, and Ahmet M. Hava. Design and performance analysis of a grid connected pwm-vsi system. In *2013 8th International Conference on Electrical and Electronics Engineering (ELECO)*, pages 157–161, 2013.

[13] Masoud Karimi-Ghartema. *Synchronous Reference Frame PLL*, pages 133–145. Wiley-IEEE Press, 2014.

[14] Sang-Hoon Kim. Chapter 7 - pulse width modulation inverters. In Sang-Hoon Kim, editor, *Electric Motor Control*, pages 265–340. Elsevier, 2017.

[15] Liang Ma, Wang Ran, and Trillion Q. Zheng. Modeling and control of three-phase grid-connected photovoltaic inverter. *IEEE ICCA 2010*, pages 2240–2245, 2010.

[16] Ritwik Majumder, Arindam Ghosh, Gerard Ledwich, and Firuz Zare. Angle droop versus frequency droop in a voltage source converter based autonomous microgrid. In *2009 IEEE Power Energy Society General Meeting*, pages 1–8, 2009.

[17] S. Mohamed, P. Jeyanthy, D. Devaraj, M. Shwehdi, and A. Aldalbahi. Dc-link voltage control of a grid-connected solar photovoltaic system for fault ride-through capability enhancement. *Applied Sciences*, 9:952, 2019.

[18] S. M. Muyeen, Mohammad Abdul Mannan, Mohd. Hasan Ali, Rion Takahashi, Toshiaki Murata, and Junji Tamura. Simulation technique application of space-vector pwm method in pscad/emtdc. In *2007 International Conference on Information and Communication Technology*, pages 1–4, 2007.

[19] Ratna Ika Putri, Sapto Wibowo, and Muhamad Rifa'i. Maximum power point tracking for photovoltaic using incremental conductance method. *Energy Procedia*, 68:22–30, 2015. 2nd International Conference on Sustainable Energy Engineering and Application (ICSEEA) 2014 Sustainable Energy for Green Mobility.

[20] Joan Rocabert, Alvaro Luna, Frede Blaabjerg, and Pedro Rodríguez. Control of power converters in ac microgrids. *IEEE Transactions on Power Electronics*, 27(11):4734–4749, 2012.

[21] R.P. Saini Sangram Bana. A mathematical modeling framework to evaluate the performance of single diode and double diode based spv systems. *Energy Reports*, 2, 11 2016.

[22] Aratrik Sarkar. *Modeling and Control of a Three Phase Voltage Source Inverter with an LCL Filter*. PhD thesis, ARIZONA STATE UNIVERSITY, 05 2015.

[23] M. G. Villalva, J. R. Gazoli, and E. R. Filho. Comprehensive approach to modeling and simulation of photovoltaic arrays. *IEEE Transactions on Power Electronics*, 24(5):1198–1208, 2009.

[24] Weidong Xiao and W.G. Dunford. A modified adaptive hill climbing mppt method for photovoltaic power systems. *2004 IEEE 35th Annual Power Electronics Specialists Conference (IEEE Cat. No.04CH37551)*, 3:1957–1963 Vol.3, 2004.

[25] W. Zhang. *Control of grid connected power converters with grid support functionalities*. PhD thesis, UPC, Departament d'Enginyeria Elèctrica, 2017.